JOURNAL OF THE AMERICAN CHEMICAL SOCIETY

Article

pubs.acs.org/JACS

Ordered Mesoporous Cobalt Oxide as Highly Efficient Oxygen Evolution Catalyst

Jonathan Rosen, Gregory S. Hutchings, and Feng Jiao*

Center for Catalytic Science & Technology, Department of Chemical and Biomolecular Engineering, University of Delaware, Newark, Delaware 19716, United States

Ⓢ *Supporting Information*

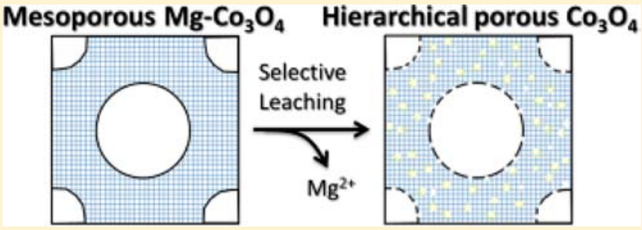

ABSTRACT: Oxygen evolution from water by use of earth-abundant element-based catalysts is crucial for mass solar fuel production. In this report, a mesoporous cobalt oxide with an ultrahigh surface area (up to 250 $m^2 \cdot g^{-1}$) has been fabricated through Mg substitution in the mesoporous Co_3O_4 spinel, followed by a Mg-selective leaching process. Approximately a third of Mg cations were removed in the leaching process, resulting in a highly porous cobalt oxide with a significant amount of defects in the spinel structure. The activated mesoporous cobalt oxide exhibited high oxygen evolution activities in both the visible-light-driven $[Ru(bpy)_3]^{2+}$−persulfate system and the Ce^{4+}/Ce^{3+} chemical water oxidation system. Under a strong acidic environment, a high turnover frequency (TOF) of ~2.2×10^{-3} s^{-1} per Co atom was achieved, which is more than twice the TOF of traditional hard-templated, mesoporous Co_3O_4.

■ INTRODUCTION

Solar fuel production from abundant sources (e.g., water and CO_2) with sunlight as the energy source is a very attractive approach toward a sustainable and clean energy future.[1−6] A range of methods, including solar thermal, photoelectrochemical, and photochemical approaches, have been proposed to produce solar fuel efficiently and economically.[1,2,7−9] Catalytic oxygen evolution from water by use of solar energy is an important reaction, because it is one of the critical reactions that are able to provide a large-scale source of electrons and protons for solar fuel production through either proton reduction to hydrogen or proton-assisted CO_2 reduction to hydrocarbons.[3,10−17] Compared to the reduction half-reaction, the oxygen evolution reaction (OER) usually has slow kinetics and requires large overpotentials. Therefore, an efficient oxygen evolution catalyst is essential to enhance the reaction rate and/or lower the overpotential.[3]

In the past few years, many earth-abundant metal oxides have been investigated as potential OER catalysts to replace expensive Ir- and Ru-based compounds.[14,18−26] Among all the catalysts, cobalt-based materials exhibited high activities in water oxidation reaction through photocatalytic and electrocatalytic approaches.[10,14,16,22,26−29] For example, Kanan and Nocera and co-workers[10,30,31] reported a Co−P_i-based electrocatalyst prepared from Co^{2+} in phosphate-containing solution through an electrodeposition process. The as-prepared Co−P_i electrocatalyst showed high activity for oxygen evolution in a neutral aqueous solution. In situ X-ray absorption study revealed that the Co−O cubane units were formed in the electrodeposition process, and these cubanes may be the active sites.[31] Another example is our recent report on cobalt oxide nanoclusters supported by mesoporous silica, which also showed high turnover frequencies (TOFs) for water oxidation driven by visible light.[32,33] The cobalt oxide nanoclusters have a typical spinel Co_3O_4 structure, which consists of Co^{2+} at tetrahedral sites and Co^{3+} at octahedral sites. In the Co_3O_4 spinel structure, octahedral cobalt and oxygen atoms form Co_4O_4 cubanes, which might be the active sites for four-electron oxygen evolution in light of the discovery of Mn_4O_4Ca as the catalytic core in nature's photosystem II. The unique property of spinel structure was also reported by Dismukes and co-workers.[34]

Mesoporous transition metal oxides are of particular interest in heterogeneous catalysis, because they combine large internal surface area, nanosized walls, and d electrons in an open shell.[35,36] In the past few years, a hard templating method has been developed and a wide range of transition metal oxides with highly ordered mesostructures have been successfully synthesized.[37−41] Some of them exhibited unique electronic, magnetic, and catalytic properties compared with their bulk and nanoparticulate counterparts.[38,40] Here, we reported a cobalt oxide-based oxygen evolution catalyst that has an ordered mesoporous structure, very high surface area, and highly crystalline spinel walls. A Mg-substituted Co_3O_4 (Mg−Co_3O_4) with three-dimensional ordered mesoporous structure was first fabricated through a hard-templating method, followed by a Mg^{2+} leaching/activation process, in which approximately a third of the Mg ions in Mg−Co_3O_4 were removed. In previous studies, lithium has been incorporated into cobalt oxide to

Received: January 17, 2013
Published: February 28, 2013

obtain favorable Co^{3+} cations and lower resistance, leading to a highly active oxygen evolution catalyst.[14,34,42] However, in this report, the role of Mg in Co_3O_4 is simply to facilitate the leaching process, which results in a cobalt oxide-based catalyst with surface area more than twice as high as that of as-made material. With a surface area up to 250 $m^2 \cdot g^{-1}$, the catalyst exhibited a much higher oxygen evolution activity than that of the mesoporous Co_3O_4 counterpart.

■ EXPERIMENTAL SECTION

Synthesis of Mesoporous Mg-Substituted Co_3O_4. Mesoporous Mg-substituted Co_3O_4 was synthesized by a method modified from a recent report by Kleitz and co-workers.[43] Preparation of mesoporous silica KIT-6 is described in the Supporting Information. In a typical synthesis of Mg−Co_3O_4, $Mg(NO_3)_2 \cdot 6H_2O$ (Sigma Aldrich, 99%) and $Co(NO_3)_2 \cdot 6H_2O$ (Sigma Aldrich, 98%) at an Mg/Co molar ratio of 2 were dissolved in a small amount of ethanol first and then mixed with mesoporous silica template (KIT-6). The weight ratio between metal precursors and silica template is approximately 2.5:1. After stirring for 1 h, the mixture was dried in an oven at 333 K overnight, before it was refluxed in dry hexane for 6 h. After the reflux process, the material was filtered and dried again in air at 333 K. The resulting dry powder was calcined at 623 K for 3 h before it was treated twice with a 2 M NaOH solution to remove the silica template. A pure Co_3O_4 spinel sample with an identical mesoporous structure was also prepared for comparison by the same synthetic approach except that no magnesium nitrate was used as precursor.

Structural Characterization. Inductively coupled plasma optical emission spectroscopy (ICP-OES) was performed at the University of Delaware Soil Testing Laboratory. Surface area and pore size measurements were measured by nitrogen physisorption on a Micrometrics Accelerated surface area and porosity system. Powder X-ray diffraction (PXRD) measurements were done on a PANaltycial X'Pert X-ray diffractometer using Cu Kα radiation. Transmission electron microscopy (TEM) and energy-dispersive X-ray spectrometry (EDX) were performed on a JEOL JEM-2010F field-emission transmission electron microscope with an accelerating voltage of 200 kV. X-ray absorption experiments were performed at beamline X10c at the National Synchrotron Light Source (NSLS) in Brookhaven National Laboratory (BNL) through the user program. The XAS data were processed using the free software IFEFFIT package, including Athena and Artemis.

Photocatalytic Oxygen Evolution from Water. Photocatalytic oxygen evolution activities of mesoporous catalysts were investigated in a well-established $[Ru(bpy)_3]^{2+}$−persulfate system.[44,45] Photocatalytic oxygen evolution activities at two different time scales were investigated in a Clark electrode system (for 2 min reaction) and a reactor−gas chromatograph (GC) setup (for 30 min reaction). In a typical Clark electrode experiment, aqueous buffer (Na_2SiF_6−$NaHCO_3$, 0.022−0.028 M) with a pH value of 5.8 was first purged with high-purity nitrogen and 2.2 mL of buffer was placed in the Clark electrode, followed by addition of 2.5 mg of catalyst, 2.5 mg of $Ru(bpy)_3Cl_2 \cdot H_2O$, 7.1 mg of $Na_2S_2O_8$, and 21.5 mg of Na_2SO_4. Before the Clark electrode system is exposed to light, a baseline is recorded for each test to guarantee no oxygen leakage or side reaction. Oxygen evolution was contiuuously monitored for at least 2 min by the Clark electrode system after exposure to a 300 W Xe research lamp (UV fused silica, 1.3 in. collimated, F/1, 1.5 in.) with a 400 nm cutoff filter. In a typical reactor−GC experiment, 40 mL of aqueous buffer (Na_2SiF_6−$NaHCO_3$, 0.022−0.028 M, pH at 5.8), 390 mg of Na_2SO_4, 130 mg of $Na_2S_2O_8$, 45 mg of $[Ru(bpy)_3]Cl_2 \cdot 6H_2O$, and 10 mg of catalyst are placed in a 127 mL reactor. The reactor was purged with high-purity helium for 10−20 min before it was irradiated with a 300 W Xe research lamp with a 400 nm cutoff filter. The oxygen concentrations in the head space after 15 and 30 min of illumination were quantitatively analyzed by a Shimadzu GC system (Shimadzu 2014). Because GC measures only the gas-phase oxygen, we assume that 4 mg/L is the dissolved oxygen concentration in the solution (i.e., half the oxygen concentration in water at room temperature).[46]

In both systems, each experiment was repeated under identical conditions at least three times to confirm the reproducibility of oxygen yield. Additional control experiments were also performed to prove that cobalt catalysts are responsible for the observed oxygen evolution activity. The absence of either cobalt catalyst or $[Ru(bpy)_3]^{2+}$ sensitizer will result in no oxygen evolution from the system.

Chemical Oxygen Evolution from Water. Chemical water oxidation experiments were performed with Ce^{4+} as sacrificial electron acceptor to oxidize water to oxygen molecules with an overpotential of ~550 mV.[18,47,48] The chemical water oxidation experiments were performed in a vessel that is attached to a Clark electrode, in which the oxygen evolution was monitored. The TOFs were calculated from the total oxygen yield after 2 min reaction. In a typical experiment, 2.0 mL of deionized water was placed in the Clark electrode system, followed by the addition of 1 mg of catalyst. The solution was bubbled with nitrogen for a few minutes to remove dissolved oxygen, followed by the addition of 0.2 mL of $(NH_4)_2Ce(NO_3)_6$ aqueous solution (2.0 M) to initiate the chemical water oxidation.

■ RESULTS AND DISCUSSION

The as-synthesized mesoporous Mg−Co_3O_4 was first examined by transmission electron microscopy (TEM), and a typical image is shown in Figure 1a. It is evident that Mg−Co_3O_4 has a well-ordered mesoporous structure, which replicates the template's three-dimensional ordered porous structure with *Ia*-3*d* symmetry, as has been shown in many other mesoporous transition metal oxides using the same hard template.[38−40] It should be noted that although a hard templating (nanocasting) method has been employed to fabricate a wide range of transition metal oxides with ordered mesostructures, the synthesis of oxides containing alkaline earth metals is still rare.[39,41] The successful preparation of Mg−Co_3O_4 with ordered mesoporous structure is further confirmed by N_2 adsorption−desorption measurements (Figure 1c). Isotherms with a typical shape for mesoporous oxides were observed, and a narrow pore size distribution centered at ~3.7 nm was obtained from the adsorption isotherm by the Barrett−Joyner−Halenda (BJH) method. A surface area of 102.1 $m^2 \cdot g^{-1}$ for Mg−Co_3O_4 was calculated from the adsorption isotherm via the Brunauer−Emmett−Teller (BET) method. These results are in good agreement with previous reports on other mesoporous metal oxides, indicating the successful synthesis of ordered mesoporous Mg−Co_3O_4.[39−41] The ordered mesoporous morphology was also confirmed by low-angle

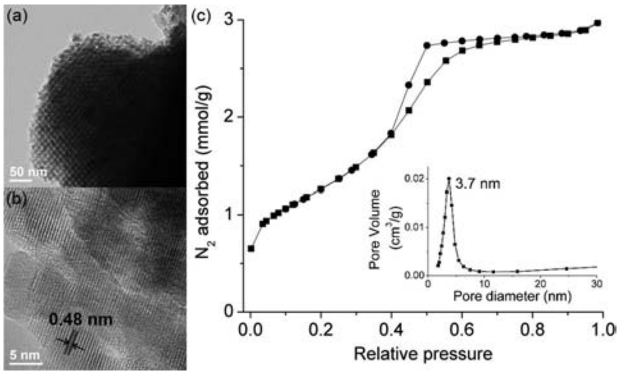

Figure 1. (a) TEM image, (b) HRTEM image, and (c) N_2 adsorption−desorption isotherms for as-synthesized mesoporous Mg−Co_3O_4. Pore size distribution (c, inset) was obtained from the adsorption isotherm (c) using the BJH method.

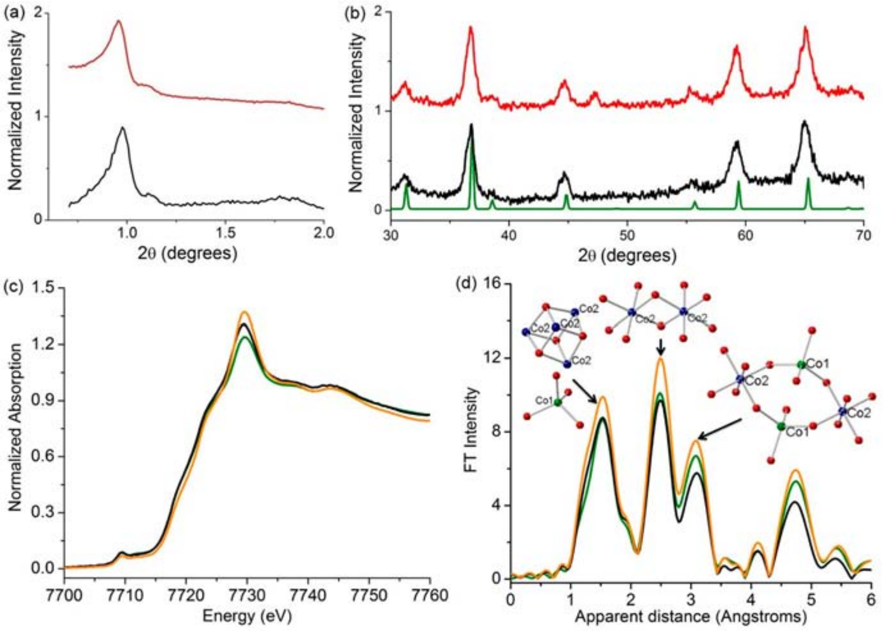

Figure 2. (a) Low-angle and (b) high-angle PXRD patterns for mesoporous Mg−Co_3O_4 (as-made, black line; postreaction, red line). The green line in panel b is the PXRD pattern for standard Co_3O_4 spinel. (c) XANES and (d) EXAFS data for as-made mesoporous Co_3O_4 (orange line) and Mg−Co_3O_4 (black line). Data for bulk Co_3O_4 (green line) are also shown for comparison.

powder X-ray diffraction analysis (PXRD), shown in Figure 2a. The as-made Mg−Co_3O_4 catalyst exhibited one well-defined sharp diffraction peak at ~1° and several weak diffraction peaks at higher angles, indicating the existence of ordered mesostructure. Mesoporous Co_3O_4 prepared under identical conditions was also characterized, and the results are in good agreement with the values reported in the literature (see Figure S1, Supporting Information).[38,49]

To examine the crystal structure of as-synthesized mesoporous Mg−Co_3O_4, high-resolution transmission electron microscopy (HRTEM) analysis has been carried out; a typical image for mesoporous Mg−Co_3O_4 catalyst is shown in Figures 1b. Clear crystal lattice fringes can be observed, suggesting the highly crystalline nature of the walls. The distance between two fringes in Figure 1b is approximately 0.48 nm, corresponding to distance between the (111) planes of Co_3O_4 spinel. The high crystallinity is further confirmed by wide-angle PXRD data in Figure 2b (black line). The diffraction pattern for as-made mesoporous Mg−Co_3O_4 closely matches the standard Co_3O_4 (green lines), confirming the success of magnesium substitution of cobalt in the spinel. The composition of mesoporous Mg−Co_3O_4 was examined by chemical analysis via inductively coupled plasma optical emission spectrometry (ICP-OES). The Mg/Co ratio in the as-prepared Mg−Co_3O_4 is 0.36, corresponding to a composition of $Mg_{0.79}Co_{2.21}O_4$. This composition is slightly off the stoichiometric ratio calculated from the metal precursors, which might be due to some magnesium being washed out during the silica template removal process using sodium hydroxide solution.

The atomic structure of mesoporous Mg−Co_3O_4 was further explored by X-ray absorption spectroscopy (XAS) analysis. All the XAS spectra were collected by use of beamline X10c at NSLS in BNL. X-ray absorption near-edge spectra (XANES) of Co K-edge (Figure 2c) confirm that both as-made mesoporous Co_3O_4 and Mg−Co_3O_4 have an identical average oxidation state of cobalt in the samples, although both Co K-edges slightly shifted to the higher energy compared to bulk Co_3O_4 spectrum, indicating the average cobalt oxidation states for both mesoporous samples are slightly higher than +2.67. In the spinel Co_3O_4, Co atoms occupy two different sites, tetrahedral and octahedral sites. The Co atoms at tetrahedral and octahedral sites are at 2+ and 3+ states, respectively. The similarity of Co oxidation states for both mesoporous samples indicates that the magnesium atoms are randomly distributed at both tetrahedral and octahedral sites in the mesoporous Mg−Co_3O_4 sample, resulting in insignificant change of the average oxidation state of Co.

Such a random distribution of Mg in the spinel structure is also confirmed by extended X-ray absorption fine structure (EXAFS) analysis. To explain the EXAFS spectra, CoO_4 tetrahedron (Co1) and CoO_6 octahedron (Co2) are shown in Figure 2d to illuminate the corresponding distances in the spinel structure. Both mesoporous materials show similar EXAFS patterns as standard Co_3O_4 in Figure 2d, while the peak intensity at ~3.1 Å (apparent distance) for as-made mesoporous Mg−Co_3O_4 is slightly lower than that for mesoporous Co_3O_4. Note that the radial distances in Figure 2d are not phase-corrected and a typical value of 0.3−0.4 Å needs to be added to convert the apparent distances into real distances.[50] After correction, the peak at 3.1 Å is now ~3.4−3.5 Å, which is close to the distance from tetrahedral Co2 to tetrahedral Co2 (3.51 Å) or from tetrahedral Co2 to octahedral Co1 (3.36 Å) in the Co_3O_4 spinel structure. Only a small reduction in peak intensity for Mg−Co_3O_4 suggests that Mg atoms are not concentrated at tetrahedral sites but randomly distributed at both sites.

The initial photocatalytic water oxidation reaction with as-made mesoporous Mg−Co_3O_4 as catalyst was performed in a Clark electrode system with $[Ru(bpy)_3]^{2+}$ as sensitizer and sodium persulfate as a sacrificial electron acceptor. The experiments were carried out at near-neutral solution (Na_2SiF_6−$NaHCO_3$ buffer with a pH value of 5.8). Because the Clark electrode measures oxygen concentration only in the liquid phase, the total reaction time was set to 120 s, beyond

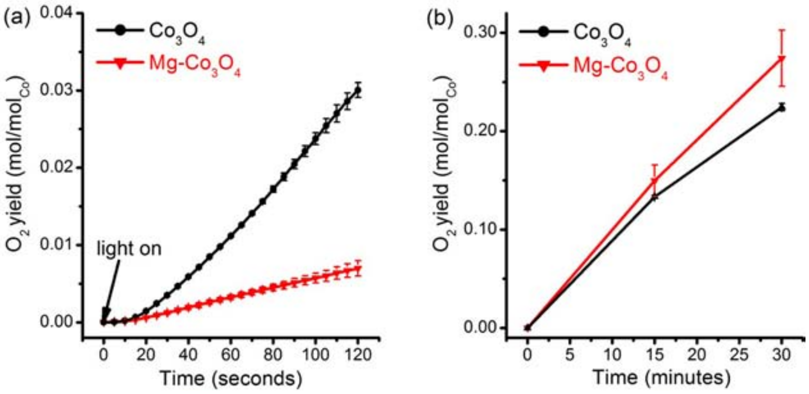

Figure 3. Oxygen yield from visible-light-driven $[Ru(bpy)_3]^{2+}$−persulfate system for mesoporous Co_3O_4 and Mg−Co_3O_4, measured by (a) Clark electrode system and (b) gas chromatography system.

which oxygen evolution goes past the saturation point. It is clear in Figure 3a that the mesoporous Co_3O_4 exhibited good oxygen evolution activity, and a TOF of 2.4×10^{-4} s^{-1} per (Co atom (~2.4×10^{-3} s^{-1} per surface Co atom) can be estimated. Such a value is similar as the TOFs [$(2.12-4.05) \times 10^{-4}$ s^{-1} per Co atom] reported for Co_3O_4 nanoclusters supported in mesoporous silica.[32,33] The TOF for mesoporous Co_3O_4 clusters is lower than the TOF for the best supported catalyst, which is likely due to two factors: (1) the mesoporous Co_3O_4 particles are strongly aggregated compared to silica-supported clusters and (2) the overall cluster size for mesoporous Co_3O_4 is much larger than supported Co_3O_4 nanoclusters, which decreases the accessibility of reagents and light. In a sharp contrast, the Mg-substituted sample showed much lower oxygen evolution activity (TOF = 5×10^{-5} s^{-1} per Co atom or 5×10^{-4} s^{-1} per surface Co atom) compared to the pure Co_3O_4 counterpart. We attribute the substantial change of activity to the Mg substitution at octahedral sites in the spinel structure, which may strongly affect the capability of Co_4O_4 cubanes to hold four electrons to produce one oxygen molecule. This observation provides us direct evidence to prove that Co_4O_4 cubane is the active site for oxygen evolution from water and that substitution of Co with alkaline metal will decrease the oxygen evolution activity significantly.

We also performed the same photocatalytic oxygen evolution in a reactor−gas chromatography (GC) combination, which allows us to extend the catalytic reaction time to 30 min. Surprisingly, the Mg−Co_3O_4 catalyst exhibited higher oxygen evolution activity (TOF = 1.6×10^{-4} s^{-1} per Co atom or 1.6×10^{-3} s^{-1} per surface Co atom) than that of pure Co_3O_4 catalyst (TOF = 1.3×10^{-4} s^{-1} per Co atom or 1.3×10^{-3} s^{-1} per Co atom) in Figure 3b. It should also be noted that the TOF for Co_3O_4 obtained from GC measurement is significantly lower than the value estimated from the Clark electrode experiment. This suggests that on a relatively small time scale the initial surface structure of the as-made catalyst plays a critical role even if it is unstable. And therefore, it quite often results in an overestimated TOF. However, if the reaction time is long enough, the catalyst will experience surface restructuring under catalytic environment and form a stable surface for prolonged catalytic oxygen evolution, and thus the initial surface structure becomes less important for long-term activity. In the case of Mg−Co_3O_4, we suspect that the Mg ions may be removed from the Mg−Co_3O_4 spinel structure, during the photocatalytic water oxidation reaction. The departure of Mg cations from octahedral sites may create defects or vacancies in the cubanes and therefore activate the catalyst. The leaching/activation mechanism is summarized in Figure 4. The reason why such activation was not observed in the Clark electrode experiments is the short reaction time (2 min) and the slow Mg leaching process in a low acidic environment (pH = 5.8). It is important to point out that after activation the Mg−Co_3O_4 catalyst stabilized itself, which was confirmed by repeating the same experiment twice with the same catalyst. After an initial 30 min of photocatalysis, we readjusted the reaction conditions to the original ones (i.e., pH was changed to 5.8 by use of $NaHCO_3$, and an additional 130 mg of $Na_2S_2O_8$ was added) and we irradiated the reactor for an additional 30 minutes. The same amount of oxygen yield was observed from the reactor (Table S1, Supporting Information), indicating good stability of the catalyst after initial activation.

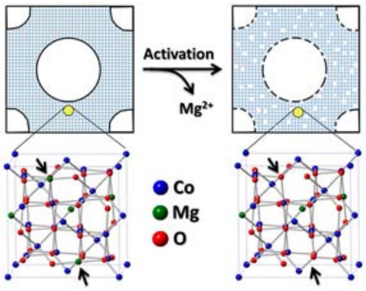

Figure 4. Schematic diagram of mesoporous Mg−Co_3O_4 through Mg cation leaching. Arrows show the Mg leaching sites (i.e., defect sites).

To elucidate the origin of the difference in activities, we recovered Mg−Co_3O_4 after water oxidation and performed detailed structural characterizations. The chemical composition of postreaction Mg−Co_3O_4 was confirmed by ICP-OES, and the Mg/Co molar ratio was reduced to 0.27 compared to the initial Mg/Co ratio of 0.36. TEM analysis shows that the ordered mesoporous Mg−Co_3O_4 is still preserved throughout the sample (Figure 5a), while the presence of significant amount of amorphous silica was also confirmed by the energy-dispersive X-ray spectroscopy (EDX) analysis (Figure 5c). Silica particle formation may be due to the hydrolysis of Na_2SiF_6 in the buffer during photolysis. The low-angle PXRD pattern for postreaction mesoporous Mg−Co_3O_4 (Figure 2a, red line) clearly shows similar peaks as the as-synthesized sample, further proving that the ordered mesoporous structure is maintained after 30 min of photocatalysis. At wide angles, the

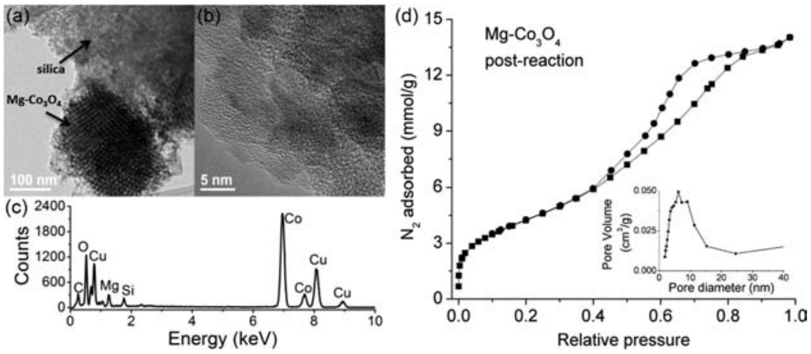

Figure 5. (a) TEM image, (b) HRTEM image, (c) EDX spectrum, and (d) N_2 adsorption−desorption isotherms for postreaction Mg−Co_3O_4 sample. The inset in panel d is the pore size distributions calculated from the adsorption isotherms. The carbon and copper signals in panel c originate from the carbon-coated copper TEM grid.

PXRD pattern for the postreaction catalyst still exhibited well-defined peaks, corresponding to Co_3O_4 spinel structure (Figure 2b, red line), consistent with HRTEM results (Figure 5b). One small additional peak at ∼46° was observed as an impurity, which cannot be indexed to any common compounds, such as cobalt oxides, magnesium oxides, ruthenium oxides, and their silicates. XANES and EXAFS experiments were also performed and the results are shown in Figure S2 in the Supporting Information. Both average oxidation states and coordination environment of Co atoms for pre- and postreaction Mg−Co_3O_4 samples are almost identical. The XAS results together with the PXRD analysis confirmed that the majority of the postreaction sample still has the spinel structure.

We measured the surface area of mesoporous Mg−Co_3O_4 after 30 min of reaction, using N_2 adsorption−desorption analysis to examine whether the potential Mg leaching affected its surface properties. The isotherms and pore size distribution for postreaction Mg−Co_3O_4 materials are shown in Figure 5d. Although the postreaction Mg−Co_3O_4 material exhibited typical isotherms for traditional ordered mesoporous materials, the postreaction sample showed a much higher BET surface area (353.1 $m^2 \cdot g^{-1}$) than the as-made sample (102.1 $m^2 \cdot g^{-1}$), which is likely due to Mg leaching during photocatalysis and the formation of high surface area silica particles. Another significant difference observed from the nitrogen adsorption experiments is the broad pore size distribution for postreaction Mg−Co_3O_4 compared to as-made material. To decouple different contributions to the increased surface area, we carried out a control experiment with mesoporous Co_3O_4 under identical conditions and examined the structure of the postreaction material (Table S2, Supporting Information). An increase of BET surface area from 106.9 to 249.3 $m^2 \cdot g^{-1}$ was observed, indicating that the Mg leaching process increases the surface area of Mg−Co_3O_4 by approximately 100 $m^2 \cdot g^{-1}$ and silica particles might be responsible for the additional 150 $m^2 \cdot g^{-1}$ surface area. To further prove the surface area contribution from silica particles, the as-made mesoporous Mg−Co_3O_4 and Co_3O_4 were treated in diluted aqueous HNO_3 solution (pH = 3) for 30 min and investigated by N_2 adsorption measurements. The BET surface areas for acid-treated Mg−Co_3O_4 and Co_3O_4 are 231.9 and 108.6 $m^2 \cdot g^{-1}$, respectively, consistent with our conclusion that the Mg leaching contributes ∼100 $m^2 \cdot g^{-1}$ surface area and the silica particles are responsible for the remaining increase in surface area.

Another important observation from the mesoporous Mg−Co_3O_4 is that the postreaction sample with a surface area of ∼250 $m^2 \cdot g^{-1}$ is much higher than that of Co_3O_4 (∼100 $m^2 \cdot g^{-1}$), while the oxygen yield of Mg−Co_3O_4 is not doubled. This phenomenon may be due to poor accessibility for the sensitizer $[Ru(bpy)_3]^{2+}$ molecules to reach the additional surface area of Mg−Co_3O_4 particles, which makes the effective surface area much lower than that estimated from N_2 adsorption measurement. To prove it, we performed chemical water oxidation experiments with Ce^{4+} as the oxidant under much more acidic conditions with a pH value of 1−2. At such a strong acidic condition, a fast activation of as-made mesoporous Mg−Co_3O_4 is expected, and therefore a Clark electrode system was used to record the oxygen yield in the solution. The results (Figure 6) clearly show that at a much lower pH the mesoporous Mg−Co_3O_4 was able to be quickly activated and exhibited a high TOF (∼2.2×10^{-3} s^{-1} per Co atom or ∼2.2×10^{-2} s^{-1} per surface Co atom) compared to those of pure mesoporous Co_3O_4 (∼1×10^{-3} s^{-1} per Co atom or ∼1×10^{-2} s^{-1} per surface Co atom) and mesoporous silica-supported Co_3O_4 (∼ 3−5 × 10^{-4} s^{-1} per Co atom or ∼3−5 × 10^{-3} s^{-1} per surface Co atom) by the same Ce^{4+} chemical oxidation method.[33] The chemical oxidation results further confirmed the proposed leaching/activation mechanism and demonstrated the high oxygen evolution activity of activated mesoporous Mg−Co_3O_4.

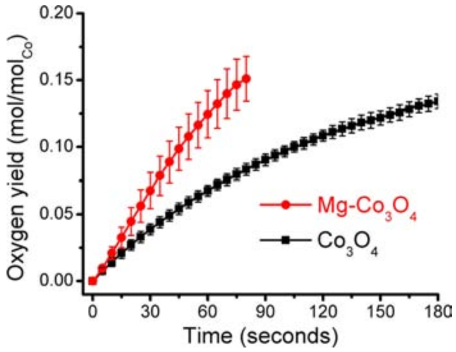

Figure 6. Oxygen yield from chemical water oxidation with $(NH_4)_2Ce(NO_3)_6$ as oxidant.

■ CONCLUSIONS

We have successfully synthesized ordered mesoporous magnesium-substituted Co_3O_4 spinel with crystalline walls. Detailed structural characterizations by HRTEM, PXRD, XANES, and EXAFS techniques show that Mg cations have been successfully substituted into both octahedral and tetrahedral sites in the Co_3O_4 spinel. Mg substitution strongly affected the oxygen evolution activities of Co_3O_4 spinel and a low TOF of 5×10^{-5} s^{-1} per Co atom ($\sim 5 \times 10^{-4}$ s^{-1} per surface Co atom) was observed. However, after prolonged oxygen evolution reaction under slightly acidic conditions (pH 5.8), the Mg in mesoporous Mg−Co_3O_4 was partially removed through a leaching process, resulting in a high surface area cobalt oxide catalyst with a much higher oxygen evolution activity (TOF = 1.6×10^{-4} s^{-1} per Co atom or 1.6×10^{-3} s^{-1} per surface Co atom). The activation of mesoporous Mg−Co_3O_4 was also studied in the chemical water oxidation reactions with a stronger acidic environment (pH at 1−2). The low-pH environment accelerated the Mg leaching process, and 1 order of magnitude higher TOF ($\sim 2.2 \times 10^{-3}$ s^{-1} per Co atom or $\sim 2.2 \times 10^{-2}$ s^{-1} per surface Co atom) was observed. The leaching/activation mechanism presented in this paper might be adapted as a general approach to fabricate metal oxide catalysts with ultrahigh surface areas and high activities.

■ ASSOCIATED CONTENT

Ⓢ Supporting Information

Two figures showing PXRD patterns and XANES and EXAFS spectra; additional text with synthetic procedure for KIT-6 and experimental details for long-term stability study; and two tables showing long-term stability testing and BET surface areas for catalysts before and after reaction. This material is available free of charge via the Internet at http://pubs.acs.org.

■ AUTHOR INFORMATION

Corresponding Author

jiao@udel.edu

Notes

The authors declare no competing financial interest.

■ ACKNOWLEDGMENTS

This work is funded by the University of Delaware startup fund. Use of the National Synchrotron Light Source, Brookhaven National Laboratory, was supported by the U.S. Department of Energy, Office of Science, Office of Basic Energy Sciences, under Contract DE-AC02-98CH10886.

■ REFERENCES

(1) Gratzel, M. *Nature* **2001**, *414*, 338.
(2) Kudo, A.; Miseki, Y. *Chem. Soc. Rev.* **2009**, *38*, 253.
(3) Hurst, J. K. *Science* **2010**, *328*, 315.
(4) Hammarstrom, L.; Winkler, J. R.; Gray, H. B.; Styring, S. *Science* **2011**, *333*, 288.
(5) Scholes, G. D.; Fleming, G. R.; Olaya-Castro, A.; van Grondelle, R. *Nat. Chem* **2011**, *3*, 763.
(6) Dahl, S.; Chorkendorff, I. *Nat. Mater.* **2012**, *11*, 100.
(7) Chueh, W. C.; Falter, C.; Abbott, M.; Scipio, D.; Furler, P.; Haile, S. M.; Steinfeld, A. *Science* **2010**, *330*, 1797.
(8) Hoertz, P. G.; Mallouk, T. E. *Inorg. Chem.* **2005**, *44*, 6828.
(9) Lewis, N. S.; Nocera, D. G. *Proc. Natl. Acad. Sci. U.S.A.* **2006**, *103*, 15729.
(10) Kanan, M. W.; Nocera, D. G. *Science* **2008**, *321*, 1072.
(11) Jiao, F.; Frei, H. *Energy Environ. Sci.* **2010**, *3*, 1018.
(12) Yin, Q. S.; Tan, J. M.; Besson, C.; Geletii, Y. V.; Musaev, D. G.; Kuznetsov, A. E.; Luo, Z.; Hardcastle, K. I.; Hill, C. L. *Science* **2010**, *328*, 342.
(13) Iyer, A.; Del-Pilar, J.; King'ondu, C. K.; Kissel, E.; Garces, H. F.; Huang, H.; El-Sawy, A. M.; Dutta, P. K.; Suib, S. L. *J. Phys. Chem. C* **2012**, *116*, 6474.
(14) Rasiyah, P.; Tseung, A. *J. Electrochem. Soc.* **1983**, *130*, 365.
(15) Wang, D. E.; Li, R. G.; Zhu, J.; Shi, J. Y.; Han, J. F.; Zong, X.; Li, C. *J. Phys. Chem. C* **2012**, *116*, 5082.
(16) Yamada, Y.; Yano, K.; Hong, D. C.; Fukuzumi, S. *Phys. Chem. Chem. Phys.* **2012**, *14*, 5753.
(17) Thomann, I.; Pinaud, B. A.; Chen, Z. B.; Clemens, B. M.; Jaramillo, T. F.; Brongersma, M. L. *Nano Lett.* **2011**, *11*, 3440.
(18) Najafpour, M. M.; Ehrenberg, T.; Wiechen, M.; Kurz, P. *Angew. Chem., Int. Ed.* **2010**, *49*, 2233.
(19) Robinson, D. M.; Go, Y. B.; Greenblatt, M.; Dismukes, G. C. *J. Am. Chem. Soc.* **2010**, *132*, 11467.
(20) Boppana, V. B. R.; Jiao, F. *Chem. Commun.* **2011**, *47*, 8973.
(21) McAlpin, J. G.; Stich, T. A.; Ohlin, C. A.; Surendranath, Y.; Nocera, D. G.; Casey, W. H.; Britt, R. D. *J. Am. Chem. Soc.* **2011**, *133*, 15444.
(22) McCool, N. S.; Robinson, D. M.; Sheats, J. E.; Dismukes, G. C. *J. Am. Chem. Soc.* **2011**, *133*, 11446.
(23) Shevchenko, D.; Anderlund, M. F.; Thapper, A.; Styring, S. *Energy Environ. Sci.* **2011**, *4*, 1284.
(24) Townsend, T. K.; Sabio, E. M.; Browning, N. D.; Osterloh, F. E. *Energy Environ. Sci.* **2011**, *4*, 4270.
(25) Gao, M. R.; Xu, Y. F.; Jiang, J.; Zheng, Y. R.; Yu, S. H. *J. Am. Chem. Soc.* **2012**, *134*, 2930.
(26) La Ganga, G.; Puntoriero, F.; Campagna, S.; Bazzan, I.; Berardi, S.; Bonchio, M.; Sartorel, A.; Natali, M.; Scandola, F. *Faraday Discuss.* **2012**, *155*, 177.
(27) Gorlin, Y.; Jaramillo, T. F. *J. Am. Chem. Soc.* **2010**, *132*, 13612.
(28) Man, I. C.; Su, H. Y.; Calle-Vallejo, F.; Hansen, H. A.; Martinez, J. I.; Inoglu, N. G.; Kitchin, J.; Jaramillo, T. F.; Norskov, J. K.; Rossmeisl, J. *ChemCatChem* **2011**, *3*, 1159.
(29) Pinaud, B. A.; Chen, Z. B.; Abram, D. N.; Jaramillo, T. F. *J. Phys. Chem. C* **2011**, *115*, 11830.
(30) Kanan, M. W.; Surendranath, Y.; Nocera, D. G. *Chem. Soc. Rev.* **2009**, *38*, 109.
(31) Kanan, M. W.; Yano, J.; Surendranath, Y.; Dinca, M.; Yachandra, V. K.; Nocera, D. G. *J. Am. Chem. Soc.* **2010**, *132*, 13692.
(32) Jiao, F.; Frei, H. *Angew. Chem., Int. Ed.* **2009**, *48*, 1841.
(33) Yusuf, S.; Jiao, F. *ACS Catal.* **2012**, *2*, 2753.
(34) Gardner, G. P.; Go, Y. B.; Robinson, D. M.; Smith, P. F.; Hadermann, J.; Abakumov, A.; Greenblatt, M.; Dismukes, G. C. *Angew. Chem., Int. Ed.* **2012**, *51*, 1616.
(35) Ying, J. Y.; Mehnert, C. P.; Wong, M. S. *Angew. Chem., Int. Ed.* **1999**, *38*, 56.
(36) Yang, P. D.; Zhao, D. Y.; Margolese, D. I.; Chmelka, B. F.; Stucky, G. D. *Nature* **1998**, *396*, 152.
(37) Tian, B. Z.; Liu, X. Y.; Yang, H. F.; Xie, S. H.; Yu, C. Z.; Tu, B.; Zhao, D. Y. *Adv. Mater.* **2003**, *15*, 1370.
(38) Jiao, F.; Shaju, K. M.; Bruce, P. G. *Angew. Chem., Int. Ed.* **2005**, *44*, 6550.
(39) Yang, H. F.; Zhao, D. Y. *J. Mater. Chem.* **2005**, *15*, 1217.
(40) Jiao, F.; Harrison, A.; Jumas, J. C.; Chadwick, A. V.; Kockelmann, W.; Bruce, P. G. *J. Am. Chem. Soc.* **2006**, *128*, 5468.
(41) Lu, A. H.; Schuth, F. *Adv. Mater.* **2006**, *18*, 1793.
(42) Lee, S. W.; Carlton, C.; Risch, M.; Surendranath, Y.; Chen, S.; Furutsuki, S.; Yamada, A.; Nocera, D. G.; Shao-Horn, Y. *J. Am. Chem. Soc.* **2012**, *134*, 16959.
(43) Yen, H.; Seo, Y.; Guillet-Nicolas, R.; Kaliaguine, S.; Kleitz, F. *Chem. Commun.* **2011**, *47*, 10473.
(44) Harriman, A.; Pickering, I. J.; Thomas, J. M.; Christensen, P. A. *J. Chem. Soc., Faraday Trans. 1* **1988**, *84*, 2795.
(45) Hara, M.; Waraksa, C. C.; Lean, J. T.; Lewis, B. A.; Mallouk, T. E. *J. Phys. Chem. A* **2000**, *104*, 5275.
(46) Truesdale, G. A.; Downing, A. L. *Nature* **1954**, *173*, 1236.
(47) Hurst, J. K. *Coord. Chem. Rev.* **2005**, *249*, 313.
(48) Liu, F.; Concepcion, J. J.; Jurss, J. W.; Cardolaccia, T.; Templeton, J. L.; Meyer, T. J. *Inorg. Chem.* **2008**, *47*, 1727.
(49) Yue, W.; Zhou, W. Z. *Chem. Mater.* **2007**, *19*, 2359.
(50) Ravel, B.; Newville, M. *J. Synchrotron Radiat.* **2005**, *12*, 537.